Physics of 3-D scattering from rippled seabeds and buried targets in shallow water

Henrik Schmidt *
SACLANT Undersea Research Centre, I-19138 La Spezia, Italy

Jaiyong Lee
Massachusetts Institute of Technology, Cambridge, MA 02139.

(Received: ; Accepted for publication:)

A new wave theory model providing consistent modeling of seabed insonification, three-dimensional target scattering, and rough seabed reverberation has been used to investigate the spatial and temporal characteristics of the multi-static scattering and reverberation from rippled, shallow water seabeds. It is shown that the highly polarized - close to monochromatic - spectral characteristics of ripple fields is associated with a reverberation environment which is highly sensitive to both frequency and insonification aspect relative to the ripples. The study suggests that significant gains in detection performance for buried objects can be achieved by band-limiting the processing to frequencies below an environmentally dependent 'cut-off' frequency. The study also confirms theoretically the intuitive advantage of insonifying the seabed along the ripple direction to reduce monostatic reverberation.

PACS numbers : 43.30Bp, 43.30Gv, 43.30Hw, 43.30Vh.

INTRODUCTION

The detection and classification of targets buried in the seabed have traditionally been performed using high-frequency sonars operating at grazing angles above critical, where the acoustic field is propagating in the vertical direction in the bottom and therefore only undergoes losses associated with the seabed transmission and the bottom attenuation. However, in shallow water such an approach is severely limited in terms of coverage, and a significant research effort has recently been focused on the potential of detecting and classifying buried objects using sonars with subcritical incidence on the seabed.

Most of this work has focused on the high frequencies (10 - 100 kHz) of traditional bottom sonars, with the scientific issues being associated with the fundamental physics of the bottom interaction. Here, one of the most important issues has been the identification of mechanisms for subcritical bottom penetration, including rough seabed scattering [1], and porous media effects [2]. Other research has focused on the seabed reverberation environment, which is obviously a critical factor in regard to sonar performance [3, 4]. Other related work has been associated with the issues of the actual scattering process for buried targets [5].

It is well known that lower frequencies have better penetration properties, in part because of the lower attenuation, but more importantly in the context of subcritical target detection, lower frequencies have a deeper evanescent 'tail' at subcritical incidence [6]. As a consequence a significant research effort has recently been directed towards lower frequencies. Thus, for example, SACLANTCEN has directed a series of bottom interaction experiments involving both penetration, reverberation, and target scattering measurements, using a parametric sonar with secondary frequencies in the range 2-12 kHz. The results of this effort are beginning to emerge. Thus, a recent modeling and analysis effort has lead to a new understanding of the dominant penetration mechanisms in this frequency regime [7]. The analysis suggests that below approximately 5 kHz the evanescent coupling is the dominant mechanism, while at higher frequencies scattering from the seabed roughness dominates.

One of the models used in Ref. [7] was the new OASES-3D scattering and reverberation model, developed at Massachusetts Institute of Technology [8, 4], and this model accurately reproduced the experimental data. Because this model inherently decomposes the field into its coherent and scattered components, it provided a direct measure of the relative contribution of the two mechanisms. Since OASES-3D inherently computes the coherent and scattered fields throughout the waveguide, the agreement with the penetration data suggested that the same model could be applied to investigate the spatial and temporal properties of the three-dimensional scattered and reverberant field in shallow water waveguides, and the principal results of this analysis are described in the following.

It should be stressed that the conclusions of this study concern only the *ripple-induced reverberation* properties. Thus, for example, at low frequencies the evanescent bottom penetration becomes significant, and scattering and

[1] On leave from: *Department of Ocean Engineering, Massachusetts Institute of Technology, Cambridge, MA 02139*

reverberation from bed-rock roughness and volume inhomogeneities such as buried rocks and boulders may become important, countering the effect of the spatial filtering provided by the seabed ripples. Also, the present study assumes the ripple field to have insignificant low-wavenumber roughness, the presence of which would increase the low-frequency reverberation levels. Another effect that will affect the signal-reverberation ratio is the frequency dependence of the sonar footprint. The present study assumes a constant sonar footprint, whereas the insonified area for parametric sonars will be approximately inversely proportional to the frequency squared, countering the predicted decay of the ripple scattering. However, the 6 dB per octave added to the low-frequency behavior of the reverberation is insignificant compared to the rapidly decaying ripple contribution. On the other hand, the beam width effect may be important in combination with the other low-frequency reverberation mechanisms.

The evaluation of the relative significance of these various mechanisms affecting low-frequency bottom reverberation requires a series of well controlled experiments incorporating different bottom types, seabed roughness statistics, and source-receiver geometries. The GOATS'98 experiment carried out jointly between SACLANTCEN and MIT in May 1998 will include measurements of the full three-dimensional reverberant field, which according to the models described here will be significantly different for the various scattering and reverberation mechanisms.

I. SCATTERING AND REVERBERATION MODEL

The 3-dimensional version of the OASES propagation model has been combined with a perturbational approach to allow full wave-theory modeling of the 3-dimensional field associated with bottom-interaction of narrow-beam sonars such as the TOPAS parametric source [9]. The new OASES-3D model handles consistently both the coherent component of the full waveguide field, including the evanescent bottom penetration, and the scattering and reverberation produced by anisotropic seabed roughness [4]. Even though the modeling approach treats the scattered field deterministically, and therefore coherently, we will maintain the traditional scattering theory terminology, with the field in the absence of scatters being referred to as the *coherent* field, and the field perturbation being denoted the *scattered* field.

As a first step, the standard OASES code is applied to compute the field in a waveguide with smooth interfaces. Subsequently, the interface scattering is computed using the perturbation approach to rough elastic interface scattering developed by Kuperman and Schmidt [10, 11]. The original perturbation theory is based on a 2-D Fourier transform formulation for rough interfaces of infinite extent. For computational reasons this approach is only feasible for evaluation of the scattered field in plane geometry with one-dimensional roughness [11]. However, many sonar problems are characterized by a sonar 'footprint' or 'patch' of limited extent, as is the case for example for the TOPAS, and an alternative implementation of the perturbation theory has therefore been devised by LePage [12], in effect representing the insonified roughness patch by a *virtual source distribution*. The field produced by this source distribution can then be very efficiently evaluated by wavenumber integration models such as OASES using azimuthal Fourier synthesis [13].

It should be pointed out that traditional perturbation approaches are most often applied to directly predict the field statistics by formal averaging. In contrast, the approach used in OASES-3D uses a spatial realization of the roughness statistics, or a directly measured roughness patch, to generate a single field realization. However, the model is sufficiently efficient to allow for computing the field statistics using Monte-Carlo ensemble averaging.

A. Coherent Field Modeling

The coherent component of the field, including the evanescent bottom field, is computed by the OASES code [8], using standard wavenumber integration for solving the fluid-elastic wave equations in stratified waveguides [6].

For arbitrary fluid-elastic stratifications, this theory decomposes the wave-field in each layer ℓ into compression and shear potentials,

$$\chi_\ell = \{\phi_\ell, \psi_\ell, \Lambda_\ell\} \tag{1}$$

where χ_ℓ is a generic potential representing the compressional potential ϕ_ℓ and the two scalar shear potentials ψ_ℓ and Λ_ℓ, representing SH and SV waves, respectively [13]. Obviously, in a fluid medium, χ_ℓ represents the compressional potential alone. For propagation and scattering in a horizontally stratified medium, it is convenient to introduce a coordinate system $(\vec{\mathbf{x}}, z)$, where the vertical coordinate z is represented by a separate scalar, while the horizontal coordinates are represented in vector form $\vec{\mathbf{x}} = (x, y)$, as indicated in Fig. 1.

Away from physical sources the seismo-acoustic field potentials of time dependence $\exp(-j\omega t)$ must satisfy homogeneous Helmholtz equations of the form

$$\left[\nabla^2 + k_\ell^2\right] \chi_\ell(\vec{\mathbf{x}}, z) = 0 \,, \tag{2}$$

where k_ℓ represents the appropriate medium wavenumbers.

In addition, the field must satisfy the boundary conditions at all interfaces z_ℓ in the stratification, as well as the source conditions. Assuming the *physical sources* are limited to a single depth, z_s, a dummy interface is added at this depth, and the interface conditions may be written in the operator form

$$B_\ell \chi_{\ell;\ell+1}(\vec{\mathbf{x}}, z_\ell) = -f_s(\vec{\mathbf{x}})\delta_{\ell s} \,, \ell = 1, 2 \cdots N \,. \tag{3}$$

where $\delta_{\ell s}$ is the Kronecker delta, having unit value at the source interface, and zero at all other interfaces. N is the total number of physical and dummy interfaces in the stratification. The differential matrix operator B_ℓ represents the derivatives relating the physical parameters involved in the boundary conditions to the potentials [10]. Thus, Eq. (3) represents the continuity of the pertinent displacements and stresses at all physical interfaces, and

discontinuity conditions imposed by the physical source distribution $f_s(\vec{\mathbf{x}}, z_s)$.

For problems with source distributions of finite horizontal extent, Eqs. (2) and (3) are most conveniently solved in cylindrical coordinates. Here, the Helmholtz equation (2) have solutions in the form of an azimuthal Fourier series of Hankel transform integrals,

$$\begin{aligned} \chi_\ell(r,z,\theta) &= \sum_{m=0}^{\infty} \left\{ \begin{array}{c} \cos m\theta \\ \sin m\theta \end{array} \right\} \int_0^\infty dk_r k_r J_m(k_r r) \\ &\times \left[\widetilde{\chi}^+_{m;\ell}(k_r) e^{jk_z z} + \widetilde{\chi}^-_{m;\ell}(k_r) e^{-jk_z z} \right] , \quad (4) \end{aligned}$$

where r, z are the depth and range coordinates, and k_r is the horizontal wavenumber. The depth-dependence of the field is represented by the exponentials, with k_z being the vertical wavenumber, defined as

$$k_z = \left\{ \begin{array}{ll} \sqrt{k_\ell^2 - k_r^2}, & k_r \le k_\ell, \\ j\sqrt{k_r^2 - k_\ell^2}, & k_r > k_\ell, \end{array} \right. \quad (5)$$

where $k_\ell = \omega / c_\ell$ is the medium wavenumber for layer ℓ. In this form, the integral representation clearly separates the field into waves *propagating* vertically in the layer ($k_r \le k_\ell$), and waves which are exponentially growing or decaying, the *evanescent* waves ($k_\ell \le k_r$), separated by the critical wavenumber $k_r = k_\ell$. The amplitudes $\chi^\pm_{m;\ell}(k_r)$ are found by matching the boundary conditions of continuous particle motion and stresses (pressure) at all interfaces in the stratification. Since these boundary conditions must be satisfied at all ranges r, they must be satisfied at each wavenumber component, in accordance with *Snell's Law*. Assembled for all interfaces these conditions are expressed in matrix form as

$$\widetilde{B}_\ell(k_r) \widetilde{\chi}^\pm_{m;\ell,\ell+1}(k_r) = -\widetilde{f}_{s;m}(k_r)\delta_{\ell s}, \ \ell = 1, 2, \ldots N \quad (6)$$

This equation is formally obtained as the Fourier-Hankel transform of the spatial boundary conditions, Eq. (3). At the depth of the source z_s, the right-hand-side represents the discontinuity of the Hankel transforms of the particle motion and pressure due to the presence of the source. Note that the global coefficient matrix $\widetilde{B}_\ell$ in Eq. (6) is independent of the Fourier order m, which has obvious computational advantages when solving for many Fourier orders. As shown by Schmidt and Glattetre [13] this is achieved by expressing the boundary conditions, and therefore the source term $\widetilde{f}_{s;m}$ in terms of the following combinations of the azimuthal expansion coefficients for the displacements and stresses:

$$\begin{aligned} \widetilde{f}_{s;m}(k_r)^T &\approx \Delta \left[(\widetilde{u}^m + \widetilde{v}^m), (\widetilde{u}^m - \widetilde{v}^m), \widetilde{w}^m, \right. \\ &\left. \widetilde{\sigma}^m_{zz}, (\widetilde{\sigma}^m_{zr} + \widetilde{\sigma}^m_{z\theta}), (\widetilde{\sigma}^m_{zr} - \widetilde{\sigma}^m_{z\theta}) \right] \quad (7) \end{aligned}$$

It should be pointed out that the wave-field amplitude solutions to Eq. (6) are *exact*, whereas the numerical evaluation of the wavenumber integrals in Eq. (4) will exhibit truncation and discretization errors. On the other hand, these errors can be reduced to insignificance by the standard wavenumber-integration contour deformation and sampling procedures [6].

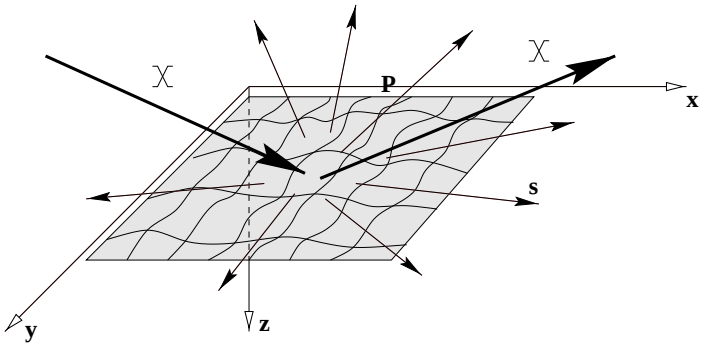

Figure 1: Rough interface patch in stratified waveguide, insonified by a seismo-acoustic field.

The OASES propagation model directly implements Eqs. (4) and (6), and consequently inherently decomposes the field into its propagating and evanescent components.

B. Perturbation Scattering Theory

Following the computation of the coherent field by wavenumber integration, the scattering by rough interfaces can be consistently handled using the method of small perturbations developed by Kuperman and Schmidt [10]. For arbitrary fluid-elastic stratifications, this theory decomposes the wave-field into coherent and scattered components of the field potentials in layer number ℓ, as illustrated in Fig. 1,

$$\chi_\ell = \langle \chi_\ell \rangle + s_\ell = \left\{ \begin{array}{lcl} \phi_\ell &=& \langle \phi_\ell \rangle + p_\ell \\ \psi_\ell &=& \langle \psi_\ell \rangle + q_\ell \\ \Lambda_\ell &=& \langle \Lambda_\ell \rangle + r_\ell \end{array} \right. \quad (8)$$

where χ_ℓ again is a generic potential representing the compressional potential and shear potentials in layer ℓ.

The coherent field satisfies the Helmholtz equation Eq. (2) and a boundary conditions similar to Eq. (3), but with a modified boundary operator B_ℓ. The self-consistent modification is important for evaluating coherent scattering losses [10]. However, for evaluating the scattered field, the unperturbed conditions may be applied for the coherent field in what is equivalent to the *Born approximation*.

Similarly, the scattered potentials satisfy homogeneous Helmholtz equations

$$\left[\nabla^2 + k_\ell^2 \right] s_\ell(\vec{\mathbf{x}}, z) = 0 \, , \quad (9)$$

and a set of boundary conditions, which according to the perturbation theory are of the form,

$$B_\ell s_{\ell;\ell+1}(\vec{\mathbf{x}}, z_\ell) = -f_v(\vec{\mathbf{x}})\delta_{\ell v} \, , \ell = 1, 2 \cdots N \quad (10)$$

where z_v is the depth of the rough interface, and the distribution function $f_v(\vec{\mathbf{x}})$ is given by [10, 11, 12]

$$f_v(\vec{\mathbf{x}}) = \left[\overbrace{\gamma_v(\vec{\mathbf{x}}) \frac{\partial B_v}{\partial z}}^{\text{elevation}} + \overbrace{\nabla \gamma_v(\vec{\mathbf{x}}) \circ b_v}^{\text{rotation}} \right] \langle \chi_{v;v+1}(\vec{\mathbf{x}}, z_v) \rangle \, . \quad (11)$$

Here, $\gamma_v(\vec{\mathbf{x}})$ is the roughness elevation of interface v at depth z_v. B_v is the same boundary operator as above, while b_v represents the rotation of the boundary conditions due to the roughness slope.

Obviously, Eq. (10) is totally equivalent to Eq. (3), with the physical source distribution $f_s(\vec{\mathbf{x}})$ replaced by the distribution function $f_v(\vec{\mathbf{x}})$ at the depth of of the rough interface. Thus, $f_v(\vec{\mathbf{x}})$ represents a *virtual source distribution*, the amplitude and phase distributions of which are determined by the coherent field and the roughness through Eq. (11)

Wavenumber Representation

For horizontal stratifications with rough interfaces of infinite extent, the perturbation theory proceeds by transforming the boundary equations (10) into the wavenumber domain, yielding for the wavenumber spectrum of the scattered field [11]

$$\begin{aligned} \widetilde{s}^{\mp}_{\ell;\ell+1}(\vec{\mathbf{q}}) &= -\widetilde{B}^{-1}_{\ell}(\vec{\mathbf{q}})\frac{\delta_{\ell v}}{2\pi}\int d^2\vec{\mathbf{k}}\widetilde{\gamma}_v(\vec{\mathbf{q}}-\vec{\mathbf{k}}) \\ &\times \left[\frac{\partial\widetilde{B}_v(\vec{\mathbf{k}})}{\partial z} + j(\vec{\mathbf{q}}-\vec{\mathbf{k}})\widetilde{b}_v(\vec{\mathbf{k}})\right]\langle\widetilde{\chi}^{\mp}_{v;v+1}(\vec{\mathbf{k}})\rangle\,, \\ &\ell = 1,2,\cdots N \end{aligned} \tag{12}$$

For random, spatially homogeneous interface roughness, the roughness statistics is given by the spatial correlation function $N_v(\Delta\vec{\mathbf{r}})$ or its Fourier transform, the normalized roughness power spectrum $P_v(\vec{\mathbf{p}})$, and the roughness variance $\langle\gamma_v^2\rangle$

$$N_v(\Delta\vec{\mathbf{r}}) = \langle\gamma_v(\vec{\mathbf{r}})\gamma_v(\vec{\mathbf{r}}+\Delta\vec{\mathbf{r}})\rangle \tag{13}$$

$$\langle\gamma_v^2\rangle P_v(\vec{\mathbf{p}}) = \frac{1}{2\pi}\int d^2\Delta\vec{\mathbf{r}}N_v(\Delta\vec{\mathbf{r}})e^{-j\vec{\mathbf{p}}\cdot\Delta\vec{\mathbf{r}}} \tag{14}$$

Then, the following expression is achieved for the spatial correlation function for the scattered field [11]

$$\begin{aligned} &C_S(\vec{\mathbf{r}}_1,z_1,\vec{\mathbf{r}}_2,z_2) = \\ &\frac{\langle\gamma_v^2\rangle}{(2\pi)^3}\int d^2\vec{\mathbf{p}}P_v(\vec{\mathbf{p}})\left[\int d^2\vec{\mathbf{q}}A_m(z_1,\vec{\mathbf{q}},\vec{\mathbf{q}}+\vec{\mathbf{p}})e^{j\vec{\mathbf{q}}\cdot\vec{\mathbf{r}}_1}\right] \\ &\times\left[\int d^2\vec{\mathbf{q}}A_n(z_2,\vec{\mathbf{q}},\vec{\mathbf{q}}+\vec{\mathbf{p}})e^{j\vec{\mathbf{q}}\cdot\vec{\mathbf{r}}_2}\right]^{\dagger} \end{aligned} \tag{15}$$

where $(\vec{\mathbf{r}}_1,z_1)$ and $(\vec{\mathbf{r}}_1,z_1)$ are the coordinates of receivers in layers m and n, respectively, and $A_m(z,\vec{\mathbf{q}},\vec{\mathbf{k}})$ is the scattering kernel

$$A_m(z,\vec{\mathbf{q}},\vec{\mathbf{k}}) = e_m(z,\vec{\mathbf{q}})\widetilde{T}^*_{v;m}(\vec{\mathbf{q}},\vec{\mathbf{k}})\langle\widetilde{\chi}^{\mp}_{v;v+1}(\vec{\mathbf{k}})\rangle$$

Here $e_\ell(z,\vec{\mathbf{q}})$ contains the exponentials representing the up- and down-going scattered wave-field in layer ℓ, and $\widetilde{T}_{v;\ell}$ is a generalized *transition-matrix* for the field in layer ℓ produced by scattering from rough interface number v,

$$\begin{aligned} \widetilde{T}_{v;\ell}(\vec{\mathbf{q}},\vec{\mathbf{k}}) &= -\widetilde{B}^{-1}_{\ell}(\vec{\mathbf{q}})\frac{\delta_{\ell v}}{2\pi}\left[\frac{\partial\widetilde{B}_v(\vec{\mathbf{k}})}{\partial z} + j(\vec{\mathbf{q}}-\vec{\mathbf{k}})\widetilde{b}_v(\vec{\mathbf{k}})\right]\,, \\ &\ell = 1,2\cdots N \end{aligned} \tag{16}$$

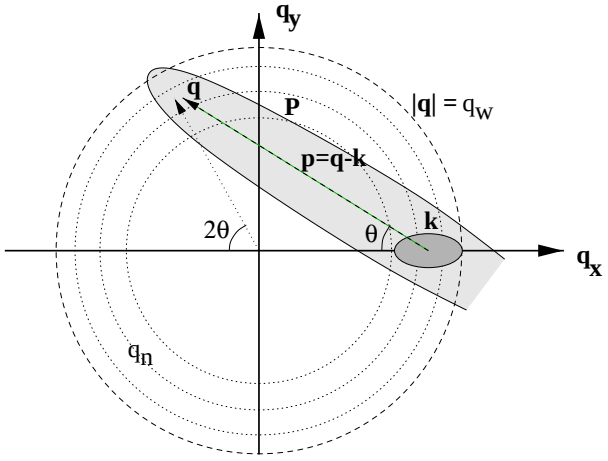

Figure 2: Graphical representation of the scattering wavenumber kernel. The scattered field is a convolution in the wavenumber plane of the incident field by the anisotropic roughness wavenumber spectrum.

The scattering integrals of both Eq. (12) and (15) are of a form convolving a medium dependent boundary operator term by the roughness spectrum at the difference wavenumber. This *Bragg scattering* condition is illustrated graphically in Fig. 2. An incident field with a wavenumber spectrum centered around the wave vector $\vec{\mathbf{k}}$ is convolved with an anisotropic roughness spectrum with skewness θ, creating a scattered field composed of wave vectors $\vec{\mathbf{q}}$ within the lightly shaded envelope in Fig. 2, representing the roughness spectrum. The modal structure of the waveguide, represented by the inverse boundary operator $\widetilde{B}^{-1}_{\ell}(\vec{\mathbf{q}})$ in Eq. 16, is indicated by the circles in Fig. 2. Thus, the resulting scattered field will have a modal structure in all directions, but shaded by the roughness spectrum centered at the incident wavenumber.

Even though in the following the wavenumber representation of the scattered field statistics is not used directly, the *Bragg scattering* condition is convenient for interpreting the numerical results, and diagrams similar to to Fig. 2 will be used extensively in the following to explain the spatial and temporal *super sensitivity* of the reverberation environment associated with rippled seabeds.

Finite Roughness Patch

For realistic two-dimensionally rough interfaces, the convolution integrals in the correlation function, Eq. (15), become four-dimensional. Even though a normal-mode expansion of Eq. (15) has recently been developed, yielding orders of magnitude in computational savings [14], the full numerical evaluation of the three-dimensional field statistics through Eq. (15) is computationally prohibitive. Consequently, numerical implementations have been limited to plane or axisymmetric problems with one-dimensional roughness [11, 14].

For a finite size roughness patch or sonar footprint, the scattered field can instead be represented by a spatial

integral over the patch P,

$$s_\ell(\vec{\mathbf{x}};z) = \int_P G_\ell(\vec{\mathbf{x}},\vec{\mathbf{x}}_v;z,z_v)d^2\vec{\mathbf{x}}_v \ , \qquad (17)$$

where $G_\ell(\vec{\mathbf{x}},\vec{\mathbf{x}}_v;z,z_v)$ is a *Generalized Green's Function* satisfying the standard Helmholtz equation, and the boundary conditions,

$$\begin{aligned} B_\ell(\vec{\mathbf{x}})G_{\ell;\ell+1}(\vec{\mathbf{x}},\vec{\mathbf{x}}_v;z,z_v) &= -\delta(\vec{\mathbf{x}}-\vec{\mathbf{x}}_v)f_v(\vec{\mathbf{x}})\delta_{\ell v} \ , \\ & \qquad \ell = 1,2\cdots N, \qquad (18) \end{aligned}$$

with the virtual source distribution $f_v(\vec{\mathbf{x}})$ given by Eq. (11). This equation is obviously of a form identical to the coherent equation, Eq. (3), and can therefore be solved in cylindrical coordinates using the Fourier-Hankel transform, with solutions of the form of Eq. (4). Inserting these solutions into Eq. (17), and reversing the order of integration, then yields for the scattered field,

$$\begin{aligned} s_\ell(r,z,\theta) &= \sum_{m=0}^{\infty} \left\{ \begin{array}{c} \cos m\theta \\ \sin m\theta \end{array} \right\} \int dq_r \ q_r J_m(q_r r) \\ &\times \left[\int_P \widetilde{G}_\ell^m(q_r,z,r_v,\theta_v) r_v dr_v d\theta_v \right] \qquad (19) \end{aligned}$$

As was the case for the coherent field produced by the physical sources, the scattered field can then be computed using the three-dimensional version of OASES [13] with the physical source kernels being replaced by the virtual source equivalents, obtained as the Fourier-Hankel transforms of Eq. (11). The details of this transformation are described by Fan [15].

The Fourier series in Eq. (19) converges very fast for orders larger than the dimensionless size ka of the patch, due to the asymptotic behavior of the virtual source kernels

$$\widetilde{G}_\ell^m(q_r,z,r_v,\theta_v) \sim J_m(q_r r_v) \to 0, \text{ for } m > q_r r_v \ , \qquad (20)$$

and the truncation of the azimuthal Fourier series is therefore easily determined *a priori*. Thus, the number of significant terms in the series depends only on the patch size with the typical number being equal to a few times the *patch size* in wavelengths. In contrast the number of terms in the numerical evaluation of each of the two dimensions of the equivalent Fourier transform in Cartesian coordinates is determined by the *receiver range*. For finite size patches, the virtual source range is typically much shorter than the receiver ranges, which is the key to the numerical superiority of the cylindrical form.

C. Target Modeling

Even though the present paper primarily focuses on the reverberation environment, the implications of the results have to be seen in the context of a potential target signal, and a generic target modeling capability has therefore been implemented into OASES-3D.

Using a 3-D adaptation of the approach of Ingenito [16], the target is represented by a *virtual source* with a radiation pattern determined by convolving the incident field by a target scattering function. The present 3-D implementation is very similar to the one recently presented by Makris[17], who rigorously derived the Fourier-Hankel representation of the 3-D waveguide field for a finite size spherical target, and then formally investigated the validity of representing the target as a *point scatterer*. Here, instead, the point-scatter assumption is directly adopted and the Fourier-Hankel transform of the scattered field is performed numerically, in a form which is directly compatible with the OASES infrastructure, totally consistent with the handling of rough interface scattering. In this *single-scattering* approach, the stratification is ignored in the actual scattering process, with the target assumed to be in an infinite medium. Thus, for an incident plane wave of wavenumber k_r and horizontal azimuthal angle θ_0, the target scattering is represented by a *shaded point source* term [16],

$$\chi(R,\theta,q_r) = \frac{\exp jkR}{R} S^{\pm}(\theta,q_r,\theta_0,k_r) \ , \qquad (21)$$

where $S^{\pm}(\theta,q_r,\theta_0,k_r)$ is the scattering function, with the $\pm$ representing the up- and downward propagating components. The scattering function is represented in terms of the horizontal wavenumbers k_r and q_r of the incident and scattered field, respectively, instead of the more common representation in terms of vertical angles. However, using the wavenumber form we can directly obtain the scattering function for evanescent incident and scattered field components by analytical continuation, which is crucial to the modeling of scattering by buried targets.

For simple objects the scattering function can be determined analytically. Thus, for spheres, the expansion of the scattering function in terms of spherical harmonics is well established [16]. The scattering function in the evanescent regime $q_r, k_r > k$ is handled by simple analytical continuation. For general targets the scattering function can be determined numerically, e.g. using finite-element approaches [18].

For a target in a stratified waveguide, Eq. (21) must be transformed into a wavenumber integral representation of the form of Eq. (4) to be able to express the boundary conditions in the wavenumber domain, Eq. (6). For the point source, corresponding to the $\exp(jkR)/R$ term in Eq. (21), this transformation is provided by the *Sommerfeld-Weil* integral, with the kernel $j\exp(jq_z|z-z_t|)/q_z$ at depth z [6]. Applying the *stationary phase* or *far-field* approximation, the corresponding wavenumber kernel for the scattered field is achieved by simply shading the kernel of the Sommerfeld-Weil integral by the scattering function,

$$\widetilde{\chi}_\ell(z,\theta,q_r) = j\frac{e^{jq_z|z-z_t|}}{q_z} S^{\pm}(\theta,q_r,\theta_0,k_r) \ . \qquad (22)$$

The wavenumber integral representation of the target scattering then follows as

$$\begin{aligned} \chi_\ell(r,z,\theta) &= \sum_{m=0}^{\infty} \left\{ \begin{array}{c} \cos m\theta \\ \sin m\theta \end{array} \right\} \int_0^{\infty} dq_r q_r J_m(q_r r) \\ &\times \ j^{m+1} \frac{e^{jq_z|z-z_t|}}{q_z} \widetilde{S}_m^{\pm}(q_r,\theta_0,k_r) \ , \qquad (23) \end{aligned}$$

where $j^m \widetilde{S}_m^{\pm}(q_r, \theta_0, k_r)$ is the Fourier-Hankel transform of the scattering function in Eq. (22). The right-hand-side of the global boundary condition equation, Eq. (6), representing the Fourier expansion terms for the scattered field then follows as the discontinuity in pressure and particle velocity above and below the nominal target depth z_t, associated with the wavenumber kernels

$$\widetilde{\chi}_{m;\ell}(q_r, z) = j^{m+1} \frac{e^{jq_z|z-z_t|}}{q_z} \widetilde{S}_m^{\pm}(q_r, \theta_0, k_r) \; . \qquad (24)$$

For incident fields of finite spectral width, the scattering function in Eq. (24) is replaced by an integral over the incident wavenumber k_r of the scattering function weighted by the spectral density of the incident field.

The solution of Eq. (6), followed by the wavenumber integration, Eq. (4), then directly yields the target scattering in all layers.

The validity of the single-scattering approach for targets near interfaces is obviously at issue, but as shown by Fawcett [5] the approach appears sufficiently accurate for objects buried in sedimentary bottoms. However, the single-scatter approximation may be inadequate when modeling the temporal details of the scattered signals. Here the late multiples may be of lower amplitude than the primary response, but separated enough in time to provide important classification information. Another related issue, in particular for objects close to the seabed interface, is the treatment of the target as a *point scatterer* which is a key feature of this approach. The validity of this approximation was rigorously addressed by Makris [17] who concluded that the point scatterer approximation for the sphere is valid for ranges in excess of a sphere diameter from the centroid. It is uncertain how this translates to the handling of transmission through the seabed interface from shallow-buried targets. However, it is hypothesized that by including the evanescent components of both the incident and scattered fields, the correct physics of the primary interaction with buried targets is adequately represented, at both super- and sub-critical sonar scenarios. In any case, all the approximations made here must ultimately be assessed by comparison to results of 'exact' numerical models and, more importantly, experiments.

II. 3-D SCATTERING AND REVERBERATION

The new scattering and reverberation model has previously been applied to investigate the mechanisms responsible for sonar penetration into rippled seabeds in the 1-10 kHz frequency regime [7]. This study showed excellent agreement between the penetration predicted by OASES-3D and the predictions of a Helmholtz-Kirchoff approach [19], and the agreement with the experimental data was excellent, both qualitatively and quantitatively. The analysis concluded that two mechanisms were primarily responsible for the subcritical penetration. At frequencies up to 5-7 kHz, the direct evanescent coupling is the controlling mechanism. This was confirmed by direct OASES [8] modeling using both plane wave and finite beam insonification of the seabed.

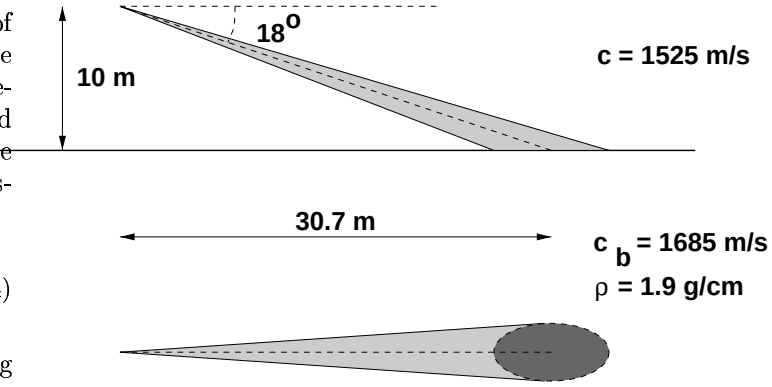

Figure 3: Geometry configuration for seabed reverberation modeling. A parametric sonar is used to insonify a seabed patch of approximately 10 × 5 m, at a nominal grazing angle of 18°.

At higher frequencies, both scattering models showed a dominance of the roughness scattering contribution. Further, the modeling showed a sharp *'cut-off'* in the scattering contribution below 3 kHz. A detailed analysis of this phenomenon showed that the unexpectedly sharp low-frequency cut-off is associated with the particular spectral characteristics of seabed ripples. Most scattering work in the past has been assuming Gaussian or power-law spectra of the seabed roughness [20], which, when adopted here, resulted in a much more gradual frequency dependence of the scattering contribution.

This understanding then lead to the hypothesis that the reverberant field in the water column would exhibit a similarly sharp low-frequency cut-off. Such a phenomenon, in combination with the low-frequency enhancement of the evanescent penetration and scattering by buried objects in turn suggests that significant gains can be achieved in subcritical detection performance by operating below the environmentally determined 'cut-off' frequency. The present study primarily focuses on the first hypothesis, i.e. the frequency dependence of the reverberation environment and its dependence on the ripple characteristics. A parallel study is dealing with the systems issues associated with the target detection problem [21].

A. Environmental Model

The environmental model is identical to the one used for the penetration study [7]. As a characteristic subcritical incidence scenario we consider the geometry shown in Fig. 3. The water sound speed is 1525 m/s, while the bottom is sand represented by a fluid half-space with compressional velocity 1685 m/s and density 1.9 g/cm^3. The corresponding critical grazing angle is 25.17°. The seabed is insonified by a narrow-beam sonar at a nominal grazing angle of 18°. The sonar footprint is approximately 10 m × 5 m.

Three different realizations of the ripple statistics are being considered, as shown in Fig. 4. They are being generated by the ripple model developed by Pouliquen *etal.* [19], based on statistics observed during the penetration experiment. The short correlation length L of the rip-

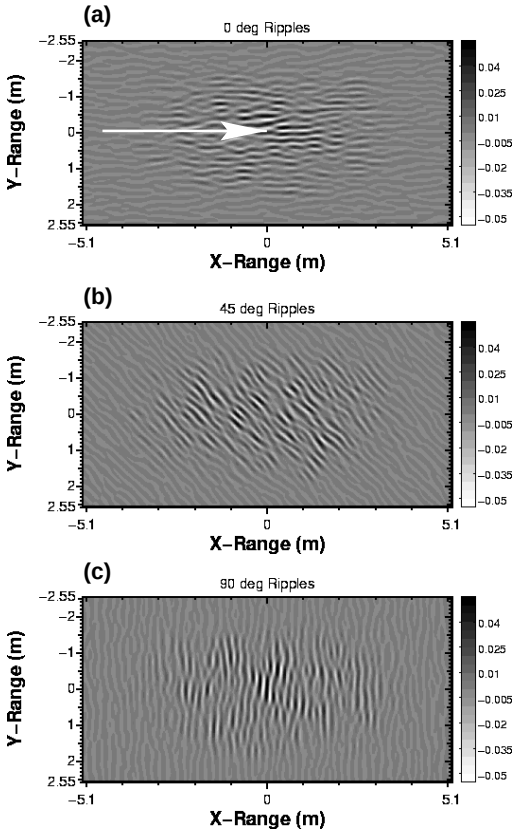

Figure 4: Rippled seabeds used for analysis. The ripples are shaded by the footprint of the sonar beam, incident at 18° grazing angle in the direction indicated by the arrow. The ripple fields are realizations of the same spectral statistics, but with different skew angles relative to the incident beam: (a) 0°; (b) 45°; (c) 90°.

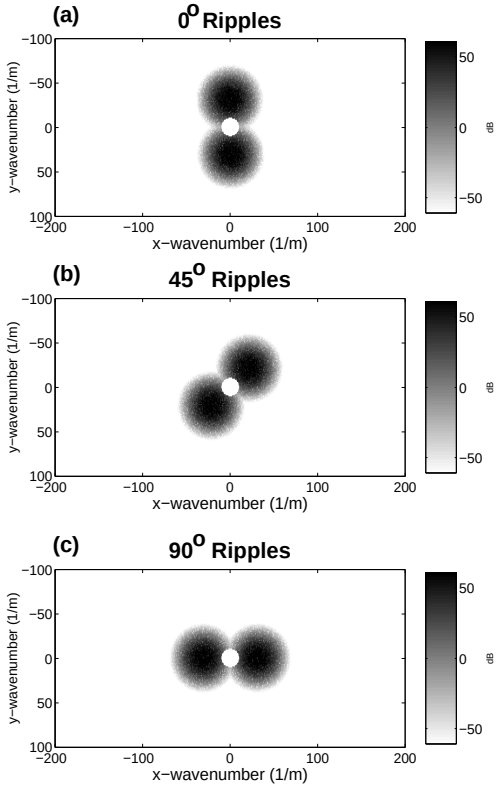

Figure 5: Wavenumber spectra in dB of rippled seabeds shown in Fig. 4. Ripple aspect angles: (a) 0°; (b) 45°; (c) 90°.

ples is 20 cm, and the RMS roughness height is 2.5 cm. Three different skewness angles are considered, 0°, 45°, and 90°. The associated roughness wavenumber spectra are shown in Fig. 5. Note the strongly polarized, almost monochromatic nature of the roughness spectra, and the filtering of the low-wavenumber components, inherent to this seabed model [19]. The very small amount of low- and high-wavenumber components of this roughness model is critical to the physics of the reverberation, as will be discussed in the following.

The roughness patches are shaded by a Hanning window consistent with the spatial width of the incident beam. The perturbation theory is linear in both the roughness γ_v and the coherent field χ_v in Eq.(11). Consequently, within the limits of the perturbation theory, the roughness shading is equivalent to a shading of the incident beam.

Even though OASES is capable of simulating the actual spectral content of the incident beam, it is much more computationally efficient to use the patch shading in combination with an incident plane wave, and the effect on the scattered field has been found to be insignificant. All the results shown in the following are therefore generated using a plane wave of unit amplitude (0dB) incident at the nominal 18° grazing.

B. Reverberant Field

The spatial and temporal distribution of the scattered field has been computed in the band 1 - 10kHz, and cov-

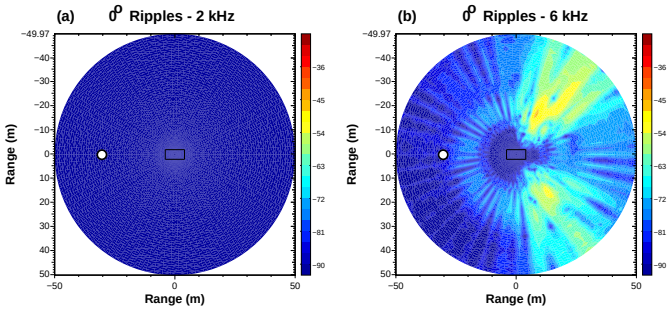

Figure 6: 3D scattering from rippled sand bottom insonified by narrow beam sonar incident at a 0° aspect angle relative to the ripple axis. The incident field is a plane wave of 0dB amplitude and 18° grazing angle. The plots show pressure level contours in dB at (a) 2 kHz and (b) 6 kHz, in a horizontal plane 10 m above the seabed, centered at the sonar footprint. The small circles indicate the position of the source and monostatic receiver for a sonar with nominal 18° grazing angle incidence. The rectangle at the origin indicates the position and size of the roughness patch.

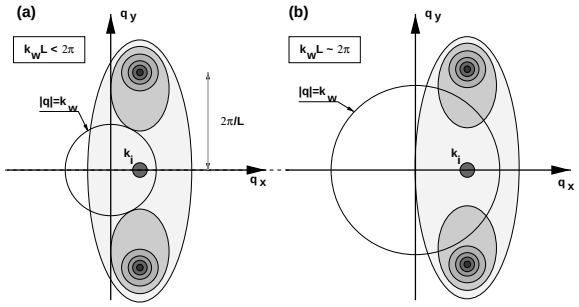

Figure 7: Bragg scattering conditions for ripples of aspect angle 0° relative to incident field. The shading indicates the level of the roughness power spectrum, centered at the incident wavenumber k_i. The short correlation length of the ripples is L, and the water wavenumber is k_w. (a) Low frequency ($k_w L < 2\pi$). (a) Medium frequency ($k_w L \approx 2\pi$).

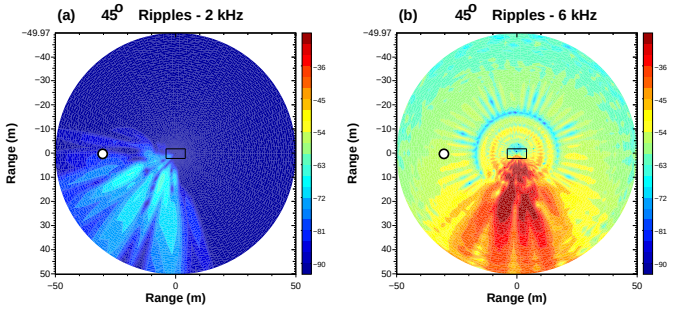

Figure 8: 3D scattering from rippled sand bottom insonified by narrow beam sonar incident at a 45° aspect angle relative to the ripple axis. The incident field is a plane wave of 0dB amplitude and 18° grazing angle. The plots show pressure level contours in dB at (a) 2 kHz and (b) 6 kHz, in a horizontal plane 10 m above the seabed, centered at the sonar footprint. The small circles indicate the position of the source and monostatic receiver for a sonar with nominal 18° grazing angle incidence. The rectangle at the origin indicates the position and size of the roughness patch.

ering ranges out to 50 m from the center of the footprint.

For the case of 0° ripples (Fig. 4(a)), Fig. 6 shows the CW power level in dB in a horizontal plane at the source depth, 10 m above the seabed, at a frequency of 2 kHz (a), and 6 kHz (b). The dimensionless correlation length of the ripples at the two frequencies are $k_w L = 2\pi f L/c = 1.6$ and 4.9, respectively. The dynamic range of the contour levels is 60 dB, with red indicating high field values and blue low. The small circle indicates the position of the source and a monostatic receiver for 18° nominal incidence. Note the extremely low reverberation levels at the low frequency, and the predominantly forward scattering at 6 kHz.

The explanation for this behavior is illustrated in Fig 7 showing the wavenumber diagram similar to Fig. 2, but consistent with the specific ripple statistics. Thus, the grey shading indicates schematically the power spectrum of Fig. 5(a), centered at the incident wavenumber k_i corresponding to 18°. The circles indicate the medium wavenumber at the two frequencies, separating the *propagating* ($q_r < k_w$) and *evanescent* components of the scattered field in the water column. At low frequencies ($k_w L < 2\pi$) most of the roughness power is outside the circle and the associated scattering is therefore evanescent in the water column and not reaching the receiver at 10 m altitude.

At the higher frequency the acoustic wavelength is of the same order of magnitude as the ripple correlation length ($k_w L \approx 2\pi$), and the 'tails' of the power spectrum enters the propagating spectrum, producing the 'splitting' in the forward scattered field observed in Fig. 6(b). The backscattering even at this high frequency is obviously still rather insignificant, consistently with Fig. 7(b).

Figure 8 and Fig. 9 show the corresponding results for the 45° ripple aspect angle in Fig. 4(b). Again the scattered field in the source plane is consistent with the Bragg conditions, with an overall increase in scattering at the higher frequency where more of the roughness power en-

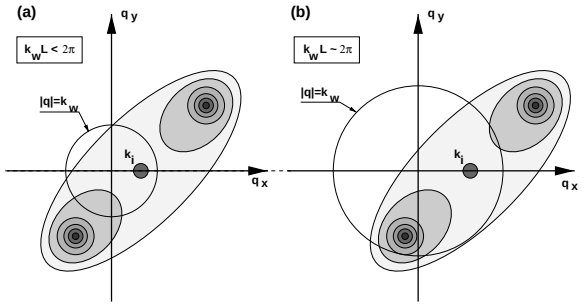

Figure 9: Bragg scattering conditions for ripples of aspect angle 45° relative to incident field. The shading indicates the level of the roughness power spectrum, centered at the incident wavenumber k_i. The short correlation length of the ripples is L, and the water wavenumber is k_w. (a) Low frequency ($k_w L < 2\pi$). (a) Medium frequency ($k_w L \approx 2\pi$).

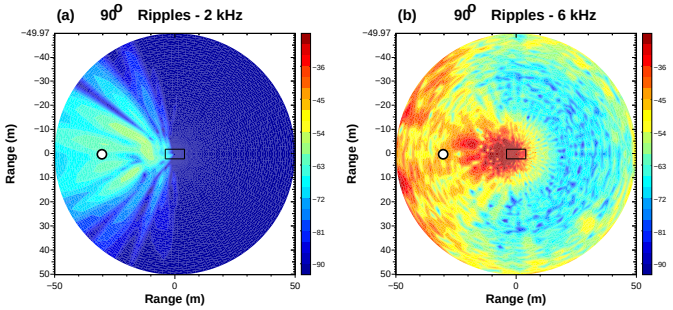

Figure 10: 3D scattering from rippled sand bottom insonified by narrow beam sonar incident at a 90° aspect angle relative to the ripple axis. The incident field is a plane wave of 0dB amplitude and 18° grazing angle. The plots show pressure level contours in dB at (a) 2 kHz and (b) 6 kHz, in a horizontal plane 10 m above the seabed, centered at the sonar footprint. The small circles indicate the position of the source and monostatic receiver for a sonar with nominal 18° grazing angle incidence. The rectangle at the origin indicates the position and size of the roughness patch.

ters the propagating regime bounded the circle $|q_r| = k_w$. The overall scattering, including the monostatic backscattering is obviously increased significantly compared to the case where the insonification is parallel to the ripples.

Finally, Figures 10 and 11 show the result for the ripples being insonified at 90°. Here the difference between the two frequencies is particularly dramatic, with a very strong backscattering observed at 6 kHz. Note also the insignificant forward scattering in this case, the reason for which is that the forward lobe of the power spectrum is in the evanescent regime, as illustrated in Fig. 11. Also, the Bragg diagrams show that for this case a maximum in the backscattering can be expected for a frequency for which $2\pi/L = 2k_i$ which translates to a frequency of f = 4.22 kHz.

C. Target Scattering

The implications of the temporal and spatial characteristics of the ripple reverberation become particularly evident when compared to the scattering produced by a

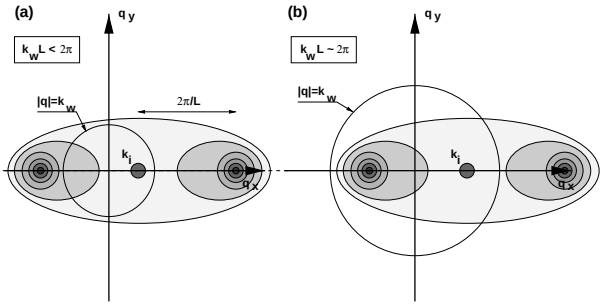

Figure 11: Bragg scattering conditions for ripples of aspect angle 90° relative to incident field. The shading indicates the level of the roughness power spectrum, centered at the incident wavenumber k_i. The short correlation length of the ripples is L, and the water wavenumber is k_w. (a) Low frequency ($k_w L < 2\pi$). (a) Medium frequency ($k_w L \approx 2\pi$).

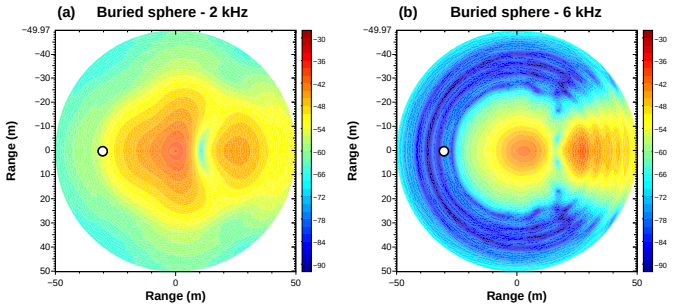

Figure 12: 3D scattering from 30 cm radius sphere buried flush in sand bottom insonified by a plane wave of 0dB amplitude and 18° grazing angle. The plots show pressure level contours in dB at (a) 2 kHz ($ka \simeq 2.2$) and (b) 6 kHz ($ka \simeq 6.7$), in a horizontal plane 10 m above the seabed, centered at the sonar footprint. The small circles indicate the position of the source and monostatic receiver for a sonar with nominal 18° grazing angle incidence.

seabed target. To illustrate this, OASES-3D has been applied to compute the 3-D scattered field produced by a solid sphere of radius 30 cm, buried flush at the center of the sonar footprint, and insonified by a plane wave of 18° incidence. Analogous to the reverberation results above, Fig. 12 shows the scattered power in dB in a horizontal plane 10 m above the seabed, centered at the target and covering ranges out to 50 m. The spatial structure of the target scattering is obviously significantly different from the reverberation. Thus, the target scattering at 6 kHz, corresponding to $ka \simeq 6.7$, shown in Fig. 12(b), is dominated by steep scattering angles, with a sharp drop in scattered power beyond a range of approximately 22 m, corresponding to the critical angle of 25.17°. At shorter ranges, the target scattering path corresponds to waves propagating in the bottom, while at longer ranges the coupling of the target scattering back into the water column is occurring through evanescent coupling, or 'tunneling'. For $r > 22$m a radial interference pattern is evident, being associated with interference between the 'tunneled' direct arrival and a second diffracted (creeping wave) arrival from the target, as discussed later in relation to the temporal response. Another characteristic feature at the higher frequency is the strong forward lobe, even in the evanescent regime.

The corresponding result at 2 kHz ($ka \simeq 2.2$) is shown in Fig. 12(a). Here the critical angle transition is much less distinct, and the scattering at the longer ranges is significantly higher than at higher frequencies. The reason for this is obviously the slower decay of the evanescent 'tail' at subcritical angles, yielding improved penetration [7], as well as more efficient energy tunneling back into propagating waves in the water column.

The most striking difference between the target scattering and the reverberation is of course the opposite frequency dependencies. Thus, from a monostatic as well as bistatic point of view, the target scattering beyond the 'critical' cone is increasing with decreasing frequency, in contrast to the reverberation, which increases dramatically with increasing frequency.

D. Monostatic Backscatter

Even though the present study has been aimed at the physics of the 3-D scattering important to multi- and bistatic sonar concepts, there are still significant operational advantages in operating in a monostatic configuration, and here the particular spectral characteristics of the sand-ripples have some interesting implications as well.

For a monostatic receiver, the results of the target and reverberation modeling for the subcritical incidence 18°, are summarized in Figure 13, showing the backscattering power versus frequency for the three different ripple polarizations as the solid curve (0°), the dashed curve, (45°), and the dotted curve (90°. The monostatic backscattering power of the flush-buried sphere is shown as a dashed-dotted curve. Note that in contrast to the backscattering strength of a free floating target, which is approximately constant above $ka \simeq 1$, the backscattering strength of the flush-buried target has a distinct maximum at $ka \simeq 1$, as-

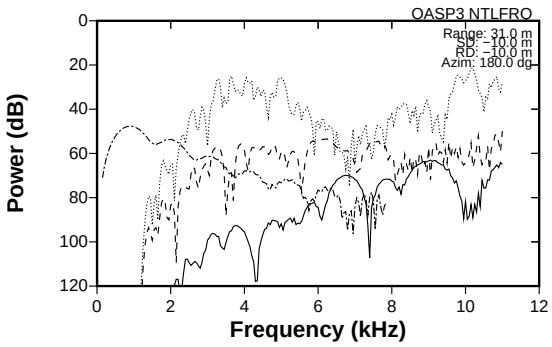

Figure 13: Frequency dependence of monostatic reverberation power for ripple aspect 0° (solid curve), 45° (dashed curve), and 90° (dotted curve), corresponding to the footprints (a), (b) and (c) in Fig. (4), respectively. The incident field is a plane wave of 0 dB amplitude and grazing angle 18°. The monostatic receiver is at 10 m altitude an 31 m range , as indicated by the small circles in Figs. (6) - (10). The dashed-dotted curve shows the monostatic target return for a sphere of 30 cm radius buried flush in a smooth seabed.

sociated with the frequency dependence of the evanescent excitation and scattering.

The dotted curve shows a clear maximum in the backscattering from the footprint at approximately 4 kHz, consistent with the Bragg condition as discussed above. Also, Fig. 13 shows a very strong dependence of the monostatic reverberation on the ripple aspect angle. Thus, at frequencies below 5 kHz the reverberation from the 90° ripples is close to 60 dB higher than from the 0° ripples, and 20-30 dB higher than the backscattering power of the 45° ripples. At frequencies above 5-7 kHz, the differences reduce to 10-20 dB.

Fig. 13 clearly illustrates the opposite frequency dependence of the buried target field and the reverberation for monostatic receivers. This in turn suggests that significant gains may be achieved in subcritical detection performance by limiting the bandwidth to frequencies below the ripple-induced 'cut-off' frequency.

Of course, Fig. 13 shows results in terms of target and reverberation power, and do therefore not account for any time-domain processing gain. To investigate the performance implications of the sonar bandwidth for buried targets, the model has been used to simulate the temporal response at a monostatic receiver. Fig. 14 shows the time series of the pressure signal, band-limited to 0.5 - 10.5 kHz. The source pulse is a replica of a Ricker wavelet with center frequency 8 kHz, commonly used for the TOPAS secondary [7]. The incident field is again a unit amplitude 18° grazing angle plane wave. The upper trace shows the pure target signal at a receiver 10 m above the seabed at 30.77 m horizontal range, corresponding to the nominal 18° grazing angle. Note the double target arrival. The first arrival is the direct target return, generated by evanescent 'tunneling' of energy back into the subcritical scattering angles. The second arrival is a diffracted arrival generated by a 'creeping wave' traveling around the spherical target. The second trace shows the simulated reverberation time series for a ripple aspect angle of 45°. Finally the lower

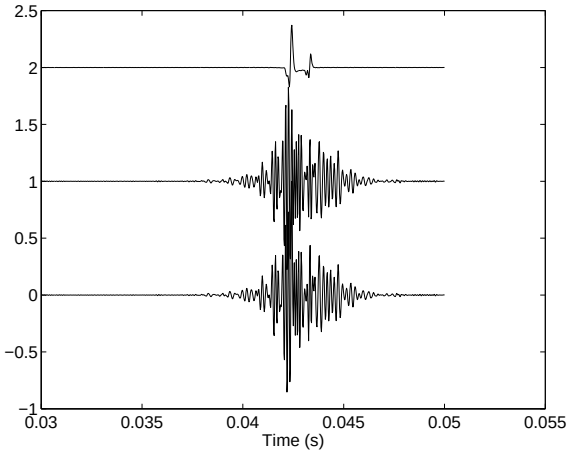

Figure 14: OASES simulation of time series of acoustic pressure at a monostatic receiver at nominally 18° grazing angle. The upper trace shows the target signal, while the center trace shows the seabed reverberation for a ripple aspect of 45° aspect. The lower trace shows the total signal. All traces are plotted on the same scale.

trace shows the total received field, where the target signal is obviously totally dominated by the reverberation.

To illustrate how the different spectral characteristics of the target and the reverberation may be explored for detection, Fig. 15 shows the spectrograms corresponding to the time series in Fig. 14. The upper plot shows contours of the spectrogram of the pure target signal, while the middle and lower plots show the spectrograms of the reverberation and the total field, respectively. Here it becomes evident that the only significant information about the presence of a buried target in this scenario is at frequencies below the reverberation 'cut-off' frequency of 2-3 kHz. This suggests that improved detection performance can be achieved by band-limiting the processing frequencies as opposed to using the full band. The investigation of this hypothesis and the associated sonar processing issues is the subject of a parallel research effort at SACLANTCEN [21].

Along the same line, the ripple orientation relative to the insonification is obviously extremely critical to the detection problem. Thus, as can be observed in Fig. 13, by insonifying along the direction of the ripples, the bandwidth associated with positive target-to-reverberation ratio is obviously increased significantly, from 2 to 6 kHz compared to the case where the insonification is perpendicular to the ripples. Also, the ripple 'wavelength' is a critical parameter. Thus, larger scale ripples encountered in deeper water will shift the reverberation 'cut-off' to a lower frequency, while shorter near-shore ripples will be associated with less low-frequency reverberation.

To take advantage of such environmental reverberation dependencies in an operational scenario, the sonar system must be closely tied to the environmental assessment and have adaptive capabilities which allows the platform to select optimal insonification and reception geometries.

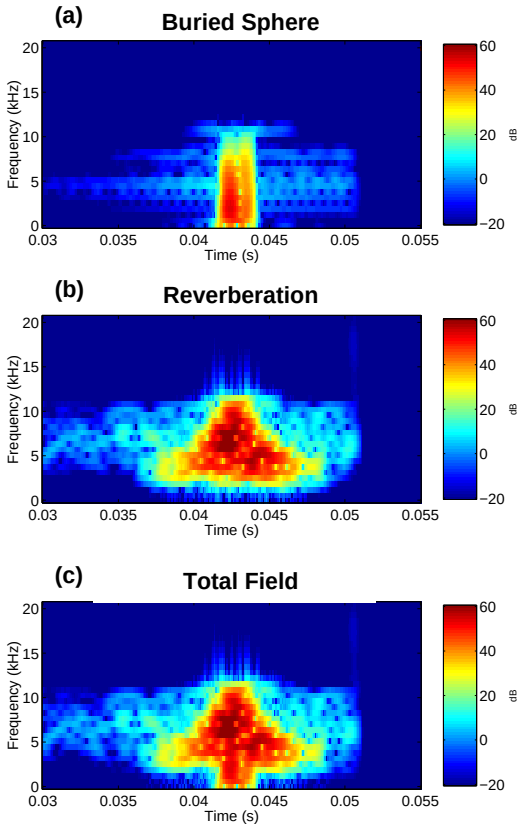

Figure 15: Spectrograms of monostatic receiver time series simulated by OASES-3D. (a) Target signal alone. (b) Reverberation for 45° ripple aspect. (c) Total signal.

III. CONCLUSION

A new wave theory model providing consistent modeling of seabed insonification, three-dimensional target scattering, and rough seabed reverberation has been used to investigate the spatial and temporal characteristics of the multi-static acoustic field associated with narrow beam sonars for seabed target detection and classification.

The reverberation environment associated with hydrodynamically induced ripple structures in water of 10-20 m depth is found to be strongly frequency dependent in the 1-10 kHz regime, with the most distinct feature being a very sharp drop in the reverberation below a 'cut-off' frequency which for sand ripples of 20 cm wavelength is approximately 2 kHz.

This low-frequency 'cut-off' feature is a result of the specific, highly polarized, roughness spectrum associated with sand ripples. Thus, the wavenumber spectrum of natural ripple fields have insignificant low-wavenumber components. In contrast, the traditional power-law roughness spectra used for characterizing seabeds have their maximum spectral content at the low wavenumbers, resulting in a more gradual reverberation decay toward lower frequencies.

In addition to the drastic drop in reverberation observed at low frequencies, the analysis also demonstrates theoretically that enhanced subcritical backscattering from buried objects is achieved at frequencies be-

low 4-5 kHz. The combined effects suggest that *enhanced detection performance can be achieved by limiting the processing bandwidth to frequencies below typically 3-4 kHz, in contrast to traditional sonar philosophy of expanding bandwidth to achieve enhanced processing gain against reverberation.*

Also, the analysis suggests, that at low frequencies in particular, a dramatic, up to 60 dB, reduction in reverberation power can be achieved by insonifying the seabed along the ripple direction.

These results in turn suggests the development of new *environmentally adaptive sonar technology* that takes optimum advantage of the strong temporal and spatial sensitivity of the seabed interaction.

However, it should be stressed that these conclusions concern only the *ripple-induced reverberation* properties. Thus, for example, it must be assumed that real ripple fields are superimposed on a finite isotropic seabed roughness which will counter the drastic low-frequency cutoff in the reverberation power predicted here, with the resultant frequency dependence of the reverberation becoming less dramatic. The relative role of such isotropic roughness components is the object of a continued modeling and experimental analysis effort, but unfortunately the low-wavenumber roughness components of real seabeds are not easily determined. On the other hand, even though the absolute reverberation levels are affected by such roughness components, the conclusions of this study are qualitatively unchanged. Also, the spatial filtering provided by the seabed ripples is countered by scattering from bedrock roughness and volume inhomogeneities such as buried rocks and boulders, which may become significant at low frequencies. Another effect that will affect the signal-reverberation ratio is the frequency dependence of the sonar footprint. The present study assumed a constant sonar footprint, whereas the insonified area for parametric sonars will be approximately inversely proportional to the frequency squared, countering the predicted decay of the ripple scattering.

The evaluation of the relative significance of these various mechanisms affecting low-frequency bottom reverberation requires a series of well controlled experiments incorporating different bottom types, seabed roughness statistics, and source-receiver geometries. The GOATS'98 experiment carried out jointly between SACLANTCEN and MIT in May 1998 will include measurements of the full three-dimensional reverberant field, which according to the models described here will be significantly different for the various scattering and reverberation mechanisms.

ACKNOWLEDGMENTS

The OASES-3D scattering and reverberation model was developed at Massachusetts Institute of Technology, supported by the Office of Naval Research, Ocean Acoustics Program.

Discussions with Kevin LePage on rough interface scattering physics, and with John Fawcett on target scattering are highly appreciated. The ripple fields used in the analysis were kindly made available by Eric Pouliquen, the discussions with whom on rough interface scattering models have also been very productive. Finally, the discussions with Alain Maguer, Edoardo Bovio, Warren Fox and Marc Pinto on target detection and classification issues are highly appreciated.

References

[1] E.I. Thorsos, D.R. Jackson, J.E. Moe, and K.L. Williams. Modeling of subcritical penetration into sediments due to interface roughness. In N.G. Pace, E. Pouliquen, O. Bergem, and A.P. Lyons, editors, *High Frequency Acoustics in Shallow Water*. SACLANTCEN Conference proceedings Series CP-45, 1997.

[2] N.P. Chotiros. Biot model of sound penetration in water saturated sand. *J. Acoust. Soc. Am.*, 97:199–214, 1995.

[3] K.L. Williams and D.R. Jackson. Bottom bistatic scattering: Experimental results and model comparison for a carbonate sediment. In N.G. Pace, E. Pouliquen, O. Bergem, and A.P. Lyons, editors, *High Frequency Acoustics in Shallow Water*. SACLANTCEN Conference proceedings Series CP-45, 1997.

[4] H. Schmidt, J. Lee, H. Fan, and K. LePage. Multistatic bottom reverberation in shallow water. In N.G. Pace, E. Pouliquen, O. Bergem, and A.P. Lyons, editors, *High Frequency Acoustics in Shallow Water*. SACLANTCEN Conference proceedings Series CP-45, 1997.

[5] J.A. Fawcett. Scattering from an elastic cylinder burried beneath a rough water/basement interface. In N.G. Pace, E. Pouliquen, O. Bergem, and A.P. Lyons, editors, *High Frequency Acoustics in Shallow Water*. SACLANTCEN Conference proceedings Series CP-45, 1997.

[6] F. Jensen, W.A. Kuperman, M.B. Porter, and H. Schmidt. *Computational Ocean Acoustics*. AIP Press, New York, 1994.

[7] A. Maguer, E. Bovio, W.L. Fox, E. Pouliquen, and H. Schmidt. Mechanisms for subcritical penetration into a sandy bottom: Experimental and modeling results. SR 287, SACLANT Undersea Research Centre, La Spezia, Italy, 1998.

[8] H. Schmidt. OASES: Version 2.1. user guide and reference manual. Technical report, Massachusetts Institute of Technology, 1997.

[9] Bentech Subsea AS, Stjørdal, Norway. *Simrad TOPAS PS 040 Operator Manual*.

[10] W.A. Kuperman and H. Schmidt. Self-consistent perturbation approach to rough surface scattering in stratified elastic media. *J. Acoust. Soc. Am.*, 86:1511–1522, 1989.

[11] H. Schmidt and W.A. Kuperman. Spectral representations of rough interface reverberation in stratified ocean waveguides. *J. Acoust. Soc. Am.*, 97(4):2199–2209, 1995.

[12] K. LePage. *Elastic scattering in oceanic waveguides*. PhD thesis, Massachusetts Institute of Technology, June 1992.

[13] H. Schmidt and J. Glattetre. A fast field model for three-dimensional wave propagation in stratified environments based on the global matrix method. *J. Acoust. Soc. Am.*, 78:2105–2114, 1985.

[14] B. Tracey and H. Schmidt. Seismo-acoustic field statistics in shallow water. *IEEE Journal of Oceanic Engineering*, 22(2):317–331, 1997.

[15] H. Fan. *Wave theory modeling of three-dimensional seismo-acoustic reverberation in ocean waveguides.* PhD thesis, Massachusetts Institute of Technology, September 1995.

[16] F. Ingenito. Scattering from objects in a stratified medium. *J. Acoust. Soc. Am.*, 82:2051–2069, 1987.

[17] N.C. Makris. A spectral approach to 3-d object scattering in layered media applied to scattering from submerged spheres. *J. Acoust. Soc. Am.*, 104:2105–2113, 1998.

[18] J. Fawcett. Finite element modelling of three-dimensional scattering from azimuthally-symmetric elastic shells. SR 273, SACLANT Undersea Research Centre, La Spezia, Italy, 1998.

[19] E. Pouliquen, A. Lyons, and N.G. Pace. Penetration of acoustic waves into sandy seafloors at low grazing angles: The helmholtz–kirchhoff approach. SR 290, SACLANT Undersea Research Centre, La Spezia, Italy, 1998.

[20] E.I. Thorsos and D.R. Jackson. The validity of the perturbation approximation for rough surface scattering using a gaussian roughness spectrum. *J. Acoust. Soc. Am.*, 86:261–277, 1989.

[21] W.L. Fox and A. Maguer. Detection of buried objects at low grazing angles: Preliminary experimental results. SR 293, SACLANT Undersea Research Centre, La Spezia, Italy, 1998.